Available online at www.sciencedirect.com
SCIENCE DIRECT®
Journal of Magnetic Resonance 169 (2004) 187–195
JMR Journal of Magnetic Resonance
www.elsevier.com/locate/jmr

Reduction of wave phenomena in high-field MRI experiments using absorbing layers

Jim Caserta,[a,*] Barbara L. Beck,[b] and Jeffrey R. Fitzsimmons[b,c]

[a] *Analog Devices, 1208 Crabtree Dr., Winston Salem, NC 27127, USA*
[b] *McKnight Brain Institute, University of Florida, P.O. Box 100015, Gainesville, FL 32610, USA*
[c] *Department of Radiology, University of Florida, P.O. Box 100374, Gainesville, FL 32610, USA*

Received 16 October 2003; revised 30 March 2004
Available online 20 May 2004

Abstract

Wave behavior, such as constructive and destructive interference, can decrease RF field homogeneity. As the static magnetic field strengths increase, these effects become more significant, resulting in image inhomogeneities. For a surface coil, wave interference is due to reflections at boundaries separating regions with largely different dielectric constants. An approach is presented to eliminate wave reflections through the use of absorbing layers. A one-dimensional plane wave model and a three-dimensional finite difference time domain numerical model at 470 MHz are presented validating the theoretical effectiveness of the approach. The findings are verified experimentally with 1 H MRI on phantoms at 11.1 T, demonstrating greatly reduced interference patterns in the images.

Keywords: FDTD; Radiofrequency; Electromagnetics; Wave interference; Simulation; Numerical calculation

1. Introduction

In the pursuit of higher signal-to-noise ratio and higher quality images, the static magnetic field (B_0) strength of MRI systems is increasing [1]. As the static field strength increases, the frequency of the RF magnetic field (B_1) increases, and the RF wavelength (λ) decreases. The wavelength decreases even further in biological tissues, since many biological samples have high relative dielectric constants (ε_r). At 470 MHz, corresponding to ^{1}H resonant frequency at 11.1 T, gray matter $\varepsilon_r = 56.2$, cerebro-spinal fluid $\varepsilon_r = 70.3$, average brain $\varepsilon_r = 48.8$ [2], and water/saline $\varepsilon_r = 78$. The electromagnetic wavelength at 470 MHz is 63.8 cm in free space, but only 9.1 cm in average brain material. As the sample dimensions represent a larger percentage of a wavelength (λ), intermediate and far-field effects, including wave propagation, become more important. The presence of intermediate and far field effects requires full-wave solutions to Maxwell's equations, either through analytical or computational means. These have been demonstrated at high static fields [3–8] and strategies have been presented to minimize these problems [9–12]. Dielectric resonance has been demonstrated in deionized water phantoms both analytically and experimentally [7,8]. However, as the sample becomes conductive the resonance is damped, and observed phenomena are more appropriately denoted as wave behavior [5].

One B_1 effect causing image inhomogeneities is wave interference. Wave interference can be either constructive or destructive. In volume coils or arrays of surface coils, multiple incident waves are available for interference. For a single surface coil, however, there is only one incident wave, but wave interference is still evident. When a sample is added, multiple propagation paths will occur from numerous reflections at the sample/air interfaces, shown in Fig. 1. Fig. 1 presents a few of the possible paths that waves could take. Fig. 1 also shows locations where these paths intersect. If, at the point of intersection, there is no phase difference between the two waves, constructive interference occurs, while if there is a 180° phase difference between the two waves,

* Corresponding author. Fax: 1-352-265-0279.
E-mail address: jim.caserta@triad.rr.com (J. Caserta).

1090-7807/$ - see front matter © 2004 Elsevier Inc. All rights reserved.
doi:10.1016/j.jmr.2004.03.027

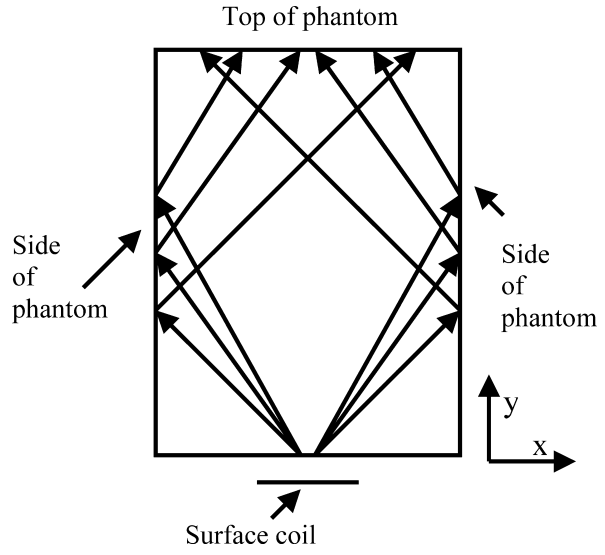

Fig. 1. Illustration of some of the multiple propagation paths that can in a rectangular sample with large reflection coefficients at material boundaries.

destructive interference occurs. Other phase differences cause different levels of interference. Fig. 1 defines the top and sides of the phantom—the top is the face opposite the surface coil, and the sides are the faces perpendicular to the surface coil.

When solving Maxwell's equations, boundary conditions are used to find an exact solution. The most significant boundary conditions are at the material boundary between the phantom and the surrounding air. Reflections occur at these material boundaries because a large reflection coefficient is present from the large difference in relative dielectric constants of the two materials (in biological tissue >40 and in air = 1). This is analogous to reflections in transmission-line theory [13]. For our uniform rectangular phantom, reflections occur at the interface between the saline phantom and air. With a surface coil, these reflected waves combine with each other and the incident wave causing interference. To reduce these interference effects, we propose reducing the wave reflections.

We propose using an additional "absorbing" layer (AL), which will absorb and dissipate the incident wave, to eliminate reflections. To dissipate the power of the incident wave, the AL must be conductive. However, a perfect conductor cannot be used because a perfect conductor would reflect 100% of the incident power, far from the situation we want. To absorb the incident wave, the dielectric constant should be as close to the sample dielectric constant as possible. A high conductivity, $\sigma = 2.0$ S/m, saline was chosen for the absorbing layer. We did not optimize the permittivity, conductivity or the dimensions of the AL. Absorbing layers are not presented as a solution for all cases, but to highlight an underlying cause of inhomogeneity. They also introduce a possible direction for improving homogeneity in high-field imaging.

The analysis in this communication covers three topics: 1D electromagnetic (EM) theory, FDTD simulations, and experimental imaging. A 1D EM theory is explored to explain the source of interference patterns when a single source is used and to demonstrate the use of absorbing layers. FDTD analysis is presented to analyze the coil–phantom system together, numerically finding a solution for the electromagnetic fields in three dimensions. The simulation environment allows a large variety of phantom sizes, while also considering the effects of excitation on the phantom as a resonator. Experimental imaging is used to confirm the interference patterns and the effects of the absorbing layers. The size of the rectangular phantom used for imaging was chosen to accentuate the interference effects seen, so the effect of the absorbing layer would be most easily demonstrated. Also, the conductivity chosen for a majority of calculations and experiments (0.25 S/m) was chosen because it has been shown to give characteristic wave patterns [5]. This conductivity is lower than most of the biological materials, but can provide insight into the general problem.

2. Materials and methods

2.1. 1D theory

To investigate the effects of sample properties and size, and also absorbing layer properties and size, we consider a plane wave normally incident on a sample. This is similar to the previous treatment given to the problem [14,15]. In the past, the total field has been described in terms of forward and reverse traveling waves [14], or by a presentation of a general form of the solution using boundary conditions to solve for the exact solution [15]. The following treatment is based on the latter approach [15] but uses different boundary conditions. We consider B_0 in the z-direction, a linearly polarized B_1 field in the y-direction (represented by a unit vector in the y-direction, $\hat{y}$), and a wave traveling in the x-direction. We use four layers, but the theory is easily extended to more. Fig. 2 shows the different layers, with their physical and electrical properties. Unlike

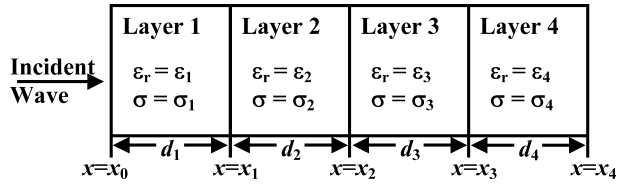

Fig. 2. Illustration of the four different layers and their physical and electrical properties.

the previous work [15], which assumes a symmetric incident wave with incoming waves from both the $+x$ and $-x$ directions, we consider an incident wave in a single direction, $\mathbf{B}(x_0) = B_{y0}\hat{y}$. A general form of the solution for the magnetic field is $\mathbf{B} = B(x)\hat{y} = B_{y0}h(x)\hat{y}$. Now, $h(x)$ is found by solving the wave equation in each layer, giving the general form:

$$h_i(x) = C_i \cos k_i x + S_i \sin k_i x \quad (1)$$

with

$$i = 1, 2, 3, 4,$$

where k_i is the complex wave number, and is defined by $k_i = \alpha_i + j\beta_i$. α_i is the attenuation constant and β_i is the phase constant in layer i [13]. The skin depth δ is related to α by $\delta = 1/\alpha$ [16]. C_i and S_i are found numerically using Matlab utilizing the eight boundary conditions: initial value at x_0, continuity of the E and B fields at x_1, x_2, and x_3, and a perfect conductor at x_4. For each of the experiments, layer 1 (the space between the source of the plane wave and the sample) is assigned free space properties. Layer 2 is the sample and its conductivity and thickness are varied. Layer 3 is assigned either the properties of either free space or an absorbing layer. Layer 4 is an absorbing boundary condition. Table 1 summarizes the conditions for three experiments. The first and second experiments investigate the damping of interference effects by (1) increasing conductivity for a fixed thickness sample and (2) increasing thickness for a conductive sample. The third experiment investigates the effects a conductive absorbing layer has on interference effects.

2.2. 3D finite difference time domain simulations

The 1D theory provides a conceptual framework to build upon, but the experimental conditions are much different. To more accurately quantify the effects of the absorbing layer, finite difference time domain (FDTD) [17–20] simulations were performed to examine B_1 behavior within the sample. The FDTD method provides a discrete-time discrete-space solution to Maxwell's equations in point form. Details of the method, theoretical treatment, and limitations are summarized elsewhere [17–20]. We used the XFDTD software package (REMCOM; State College, PA) for all FDTD simulations. The FDTD grid is composed of $150 \times 150 \times 150$ $(2.5\,\text{mm})^3$ cells, yielding a total simulation space of $(37.5\,\text{cm})^3$. Calculations at 10,000 time-steps of 4.81 ps, were performed for 22 total cycles of the input signal. Each simulation uses 95 MB of RAM and has an estimated calculation time of 71 min when performed on a 2.8 GHz Intel Xeon Processor. The fields at a specific point were observed to ensure a steady-state solution was reached. Transient field values were saved 0.532 ns apart (1/4 period at 470 MHz) to determine the steady-state magnitude and phase (complex amplitude) of the B_1 field in the x, y, and z directions.

Specifying B_0 in the z-direction, the complex amplitudes in the x and y directions are used to compute the complex amplitudes of the two circularly polarized components of B_1, $\hat{B}_1^+$, and $\hat{B}_1^-$ [3,5]. The simulated signal intensity in each pixel n, $A_{\text{pixel}}(n)$, is determined using the positively rotating field at pixel n, $\hat{B}_{1n}^+$, and a scaling factor, V, for transmission dependence, and the negatively rotating field at pixel n, $\hat{B}_{1n}^-$ for reception dependence:

$$A_{\text{pixel}}(n) = \mid \sin(V \mid \hat{B}_{1n}^+ \mid \gamma\tau) \mid \hat{B}_{1n}^- \mid\!\mid. \quad (2)$$

The transmission scaling factor, V, is determined in two different ways. First, we specify a 90° flip angle at a location of 0.25 cm into the phantom in the y (vertical in-page) direction, and in the center of the phantom in the x (horizontal in-page) direction, point 75, 49, and 75 in our simulation space. The equation is given by $V_{90} = \pi/(2 \mid \hat{B}_{1n}^+ \mid \gamma\tau)$. Second, we compute the amplitude of the free-induction decay (FID) signal, A_{FID}, for a large range of V. We then choose the value for V that yields the first relative maximum of A_{FID}, following a previously published method [19].

Two different groups of phantom loads are used. The first sample matches our experimental phantom, and is a $10.5 \times 10.5 \times 14.0$ cm rectangular box. The size of the box was chosen to be approximately $1.5 \times 1.5 \times 2\,\lambda$. This sample is filled with saline, with $\varepsilon_r = 78$ and $\sigma = 0.25$ S/m. Saline absorbing layers, with $\varepsilon_r = 78$, $\sigma = 2.0$ S/m, and 1.5 cm thick are added to either the top of the sample, all four sides of the sample, or both the top and the sides. Additionally, the simulations with absorbing layers on the sides of the sample are replicated with 0.5 cm free-space region between the sample and the absorbing layers. The model with the free-space regions matches the actual experiment; however, the model with no space

Table 1
Experimental conditions for 1D theoretical analysis

Exp. #	Layer 1			Layer 2			Layer 3			Layer 4		
	σ	ε_r	d	σ	ε_r	d	σ	ε_r	d	σ	ε_r	d
1	0	1	25	0, 0.25, 0.5, 0.75	78	10.5	0	1	25	0.1	1	50
2	0	1	25	0.25	78	10.5, 21.0, 31.5	0	1	25	0.1	1	50
3	0	1	25	0, 0.25, 0.5, 0.75	78	10.5	1	78	3.5	0.1	1	50

between the sample and absorbing layer is also important as it may be possible to build absorbing layers contained in membrane-like materials with negligible space between absorbing layer and sample.

One of the advantages of simulation over experimental imaging is the ability to rapidly change parameters. From the dielectric resonator analysis, the size of the sample determines the resonant frequencies of all modes. As the operating frequency approaches a mode frequency, the interference effects become more prominent. To investigate this effect, our second group of phantom loads are cubical with side length varying from 7.5 to 12.5 cm in 0.5 cm steps. Each cubical phantom size is then simulated with 2.5 cm wide absorbing layers on the sides of the phantom. Two absorbing layer conductivities were used: $\sigma = 1.0$ S/m and $\sigma = 2.0$ S/m. The same coil is used as with the rectangular phantoms and the coil is separately tuned for each size load.

The transmit-receive coil used is a 5×5 cm square loop placed 0.5 cm below the sample. The loop has eight breaks, one for the source and seven for tuning capacitors. The coil is tuned to 470 MHz, with the input impedance is calculated by XFDTD.

To explore the effect of the absorbing layers on signal to noise ratio, we consider the calculation from XFDTD of the total input power, P_{tot}. Total input power is equal to the sum of dissipated and radiated power. The noise is considered to be proportional to the square-root of the total input power. The total signal-to-noise ratio is computed by summing the calculated image intensity of all N pixels and dividing by the square root of the total input power, P_{tot}.

The SNR is also computed for each pixel and comparisons made along the coil axis. Also, SNR at particular points is compared for different phantom sizes and absorbing layer conditions.

2.3. Experimental imaging

We acquired experimental images using a 11.1 T/40 cm imaging system (Magnex magnet with Bruker console) [21] with spin-echo parameters: TR/TE = 500/30 ms, matrix = 512×512, FOV = 20×20 cm, bandwidth = 100 kHz, 6 slices per scan, and slice thickness = 1 mm. Power settings were chosen so that no over-tipping occurred while maintaining adequate SNR. Since 90° flip-angles were not obtained, no direct SNR comparison is made between images. The boxes containing the sample and absorbing layer phantoms had plexiglass walls 2 mm thick. 5×5 mm reinforcing beams, which also provided increased adhesive surfaces, were added to all 12 edges. The size of the sample and AL boxes is the same as in the 3D FDTD simulations. The coil was tuned and matched when loaded with the sample box. The addition of the absorbing layers had a negligible effect on tuning and matching.

3. Results and discussion

3.1. 1D theory

The effect of sample conductivity on wave interference is shown in Fig. 3. As shown in previous studies [5,8], as the sample conductivity increases, interference effects decrease. Both the incident and reflected waves are increasingly attenuated as σ increases. The sample is 10.5 cm thick in each of the four curves. Fig. 4 shows the effect of increasing sample thickness. As sample thickness increases, interference effects again decrease. The incident and reflected waves are increasingly attenuated as the distance traveled increases. Fig. 5 illustrates the

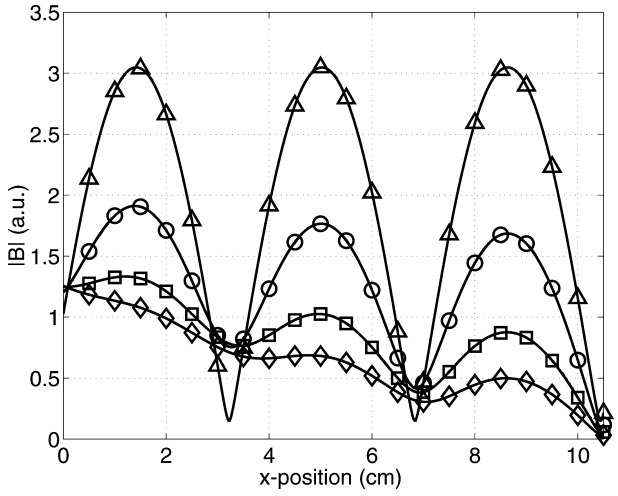

Fig. 3. 1D calculations of B_1 along the x-direction for a four-layer model without absorbing layer, for $\sigma = 0$ S/m (triangles), $\sigma = 0.25$ S/m (circles), $\sigma = 0.50$ S/m (squares), and $\sigma = 0.75$ S/m (diamonds).

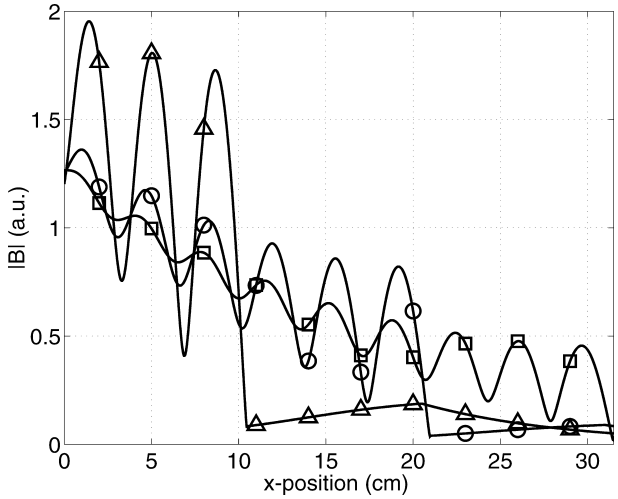

Fig. 4. 1D calculations of B_1 along the x-direction for a four-layer model without absorbing layer illustrating the effect on sample thickness. Cases shown are: d2 = 10.5 cm (triangles), d2 = 21.0 cm (circles), and d2 = 31.5 cm (squares).

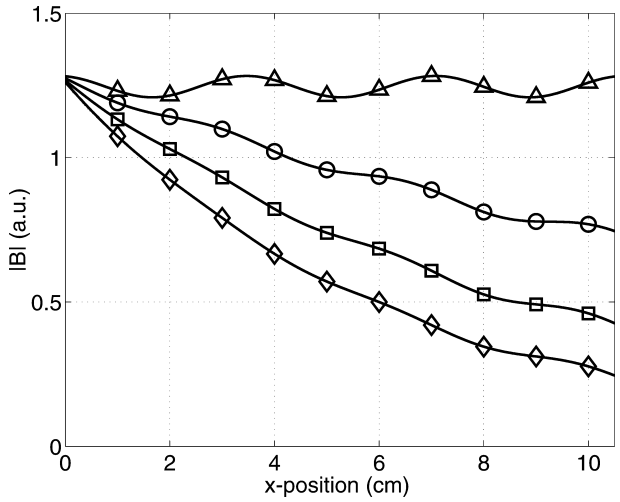

Fig. 5. 1D calculations of B_1 along the x-direction for a four-layer model with absorbing layer showing effects of sample conductivity. Cases shown are: $\sigma = 0$ S/m (triangles), $\sigma = 0.25$ S/m (circles), $\sigma = 0.50$ S/m (squares), and $\sigma = 0.75$ S/m (diamonds).

effect of the absorbing layer. The sample thickness is 10.5 cm in each curve. A standing wave pattern is apparent for the non-conductive sample, however, the ratio of its maxima to minima is 1.06 compared to 20.33 without the AL. For each of the conductive cases, the standing wave effects are nearly eliminated. These results show that for a normally incident plane wave, conductive absorbing layers are effective in reducing wave reflections and interference. Without interference, B_1 decreases monotonically as you move away from the source. This is the case at low-frequencies as you move away from a surface coil.

3.2. 3D FDTD simulations

Axial surface plots of the calculated image intensity for the rectangular phantoms are shown in Figs. 6A–D. Both the positive and negatively rotating circularly polarized components are used to calculate image intensity [4,22]. Fig. 6A, no AL, shows significant interference patterns. Fig. 6B, AL on top, shows a different, but still

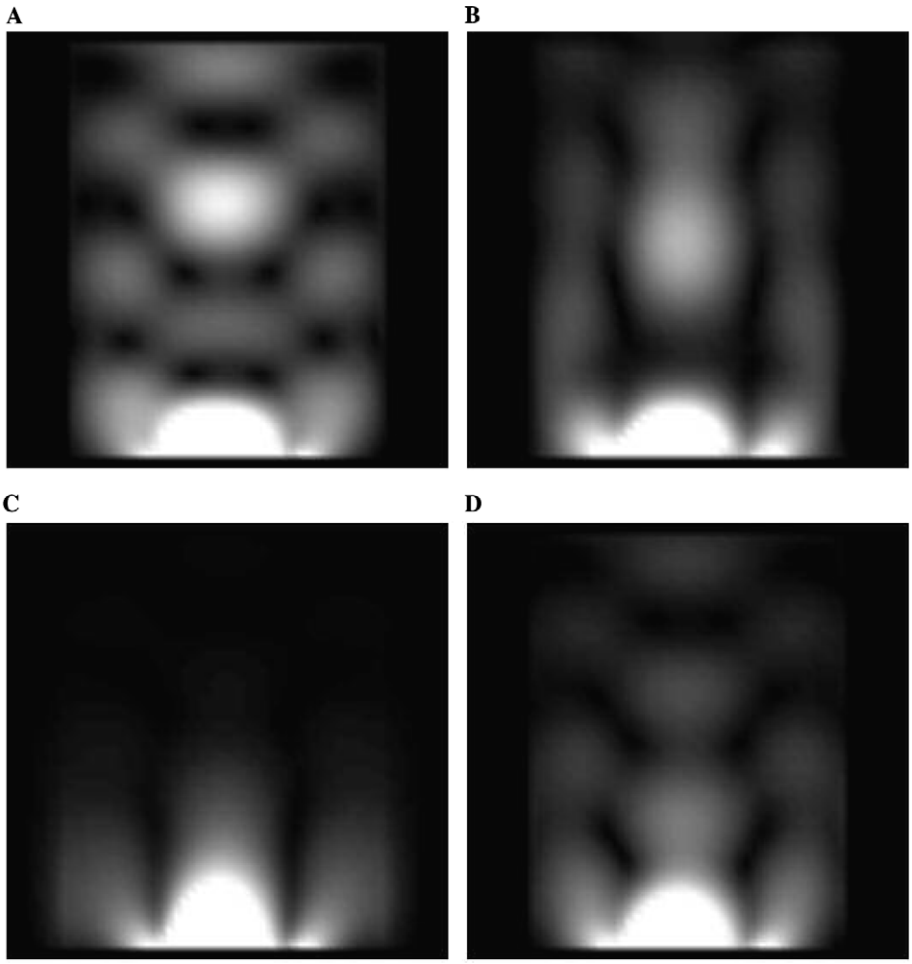

Fig. 6. FDTD calculated image intensity for (A) no AL, (B) AL on top, (C) AL on sides, and (D) AL on sides with 0.5 cm gap between AL and sample. The surface coil is below the phantom for each case.

significant interference pattern. Fig. 6C, AL on sides, shows no noticeable interference effects. Fig. 6D, AL on sides with 0.5 cm gap between phantom and AL, shows diminished interference effects. Placing the AL on both the sides of the phantom and on the top of the phantom, had effects on the interference pattern. Substantial reflections are occurring on all five faces. Placing the AL on the sides of the phantom had a larger effect than placing the AL on the top of the phantom. This could be due to either the loop coil radiation pattern or the difference in distances from top to bottom and from side to side of the phantom.

Fig. 7 shows the image intensity along a line defined by $x = 75$, through the center of the sample. When the AL is placed on the sides, the profile resembles that of a low-frequency, near-field surface coil. For the other three cases, no AL, AL on top, and AL on sides with gap, standing wave patterns are apparent. The effect is diminished for the cases with AL on top and AL on sides with gap. The case with the AL on sides with gap proves more effective at reducing the wave effects than the case with AL on top. The standing wave pattern for the cases without AL and AL on top improves sensitivity at $y = 80$. However, at $y = 60$ it is worsened considerably. The location of these improvements depends on the dielectric properties and geometric dimensions of the load. Both of these quantities are quite variable, and thus the areas of improvement would vary from scan to scan. One advantage of using the absorbing layers is removing the interference effects, and making the field distributions more predictable.

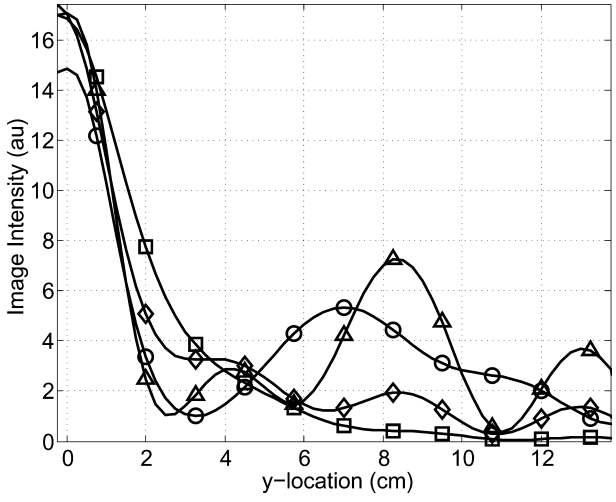

Fig. 7. Field profile showing effect of AL for no AL (triangles), AL on top (circles), AL on sides (squares), and AL on sides with 0.5 cm gap between AL and sample (diamonds).

Table 2 and Figs. 8 and 9 show the simulation results using cubical phantoms. Table 2 shows that total SNR is always decreased by the presence of the absorbing layer. However, it also shows, along with Fig. 9, that the SNR for a particular pixel may be increased by using the absorbing layer. Table 2 shows that, for the cubical phantom with side lengths 9.0–10.5 cm, the local SNR, 2 cm deep perpendicular to the coil, is improved with the AL. In one case, with side length = 9.5 cm, the improvement is over 200%. Table 2 also shows that the two different conductivity absorbing layers yield similar results.

Fig. 8 shows the basic improvement achieved with the AL—predictability of the field pattern. Fig. 8C shows an area of 3 cm into the sample where the image intensity approaches 0, while with AL the image intensity is still significant. This illustrates the most severe effect of destructive interference—complete signal cancellation.

Fig. 9 illustrates how the location of constructive interference is dependant on the size of the sample. Three points of interest are chosen, in the center of the sample in the x-direction, and 1, 2, and 3 cm deep in the y-direction. All the three show sample sizes where the SNR at each location is greater than the absorbing layer case, and sizes where the SNR is less than the absorbing layer case. In comparing the case without absorbing layer to the case with 2.0 S/m absorbing layer, large variations are seen. Fig. 9A (1 cm depth) shows a 12% increase for the 7 cm/side phantom, but a 50% decrease for the 9 cm/side phantom. Fig. 9B (2 cm depth) shows a

Table 2
SNR results for cubical phantoms without AL, with AL having $\sigma = 2.0$ S/m and with AL having $\sigma = 1.0$ S/m

Phantom side length (cm)	Total SNR			SNR at point of interest		
	No AL	AL, $\sigma = 2.0$	AL, $\sigma = 1.0$	No AL	AL, $\sigma = 2.0$	AL, $\sigma = 1.0$
7.5	1.00	0.63	0.62	1.00	0.86	0.82
8.0	1.00	0.62	0.60	1.00	0.68	0.60
8.5	1.00	0.54	0.50	1.00	0.72	0.64
9.0	1.00	0.57	0.52	1.00	1.18	1.12
9.5	1.00	0.71	0.66	1.00	3.31	3.41
10.0	1.00	0.84	0.81	1.00	2.10	2.25
10.5	1.00	0.88	0.87	1.00	1.33	1.39
11.0	1.00	0.80	0.80	1.00	1.01	0.99
11.5	1.00	0.71	0.71	1.00	0.77	0.75
12.0	1.00	0.70	0.69	1.00	0.82	0.82
12.5	1.00	0.63	0.62	1.00	0.86	0.82

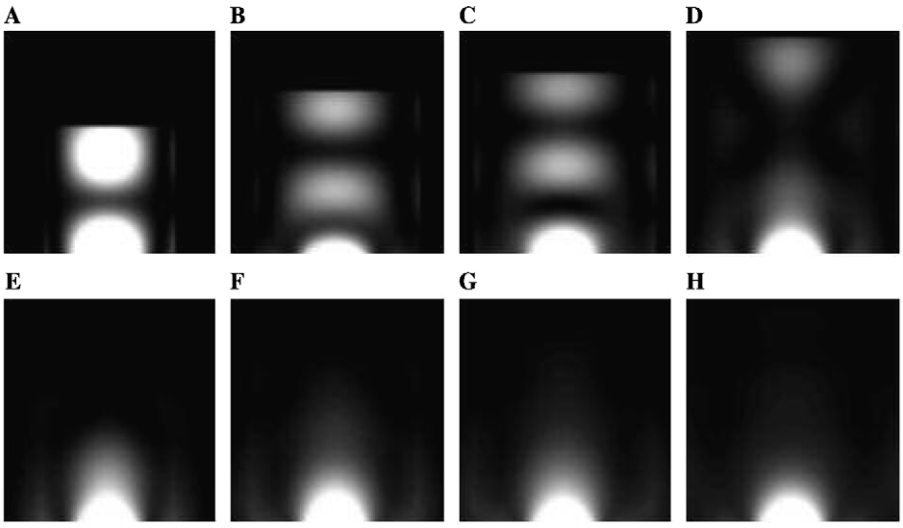

Fig. 8. Simulated sagittal images for cubical phantom side lengths of 7.5 (A,E), 9.5 (B,F), 10.5 (C,G), and 12.5 (D,H) cm. (A–D) are without AL (E–H) are with AL.

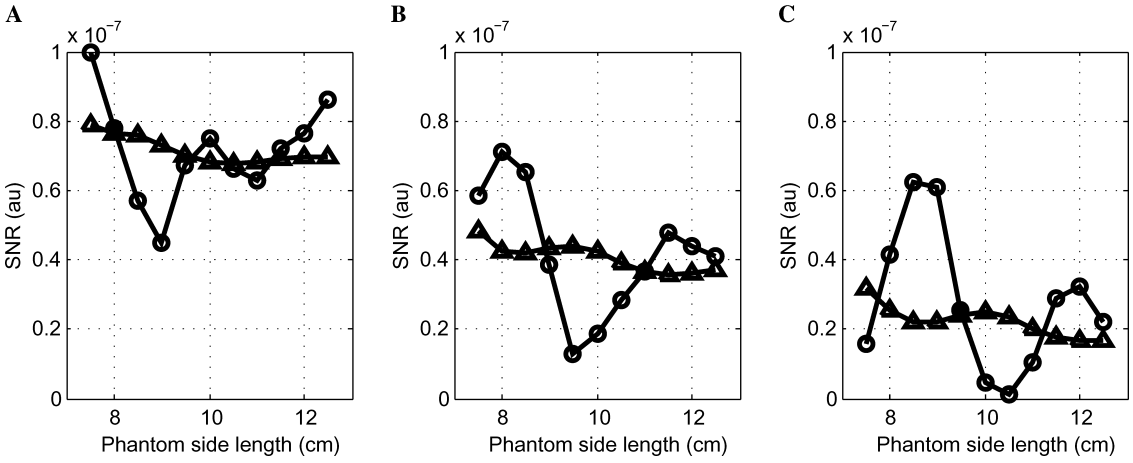

Fig. 9. SNR for cubical phantom simulations at points centered along the x axis and 1 cm (A), 2 cm (B), and 3 cm (C) deep along the y axis for the cases without AL (circles) and with $\sigma = 2.0$ S/m AL (triangles).

40% increase for the 8 cm/side phantom, but a 75% decrease for the 9.5 cm/side phantom. Fig. 9C (3 cm depth) shows a 100% increase for the 8.5 cm/side phantom, but a near 100% decrease (complete signal cancellation) for the 10.5 cm/side phantom. These results show that without the absorbing layer wave interference causes SNR to be highly unpredictable. As both the size of the sample imaged and the location of interest vary from scan to scan, more predictability and repeatability are required for practical imaging experiments.

3.3. Experimental imaging

Figs. 10A and B show two axial slices, (a) without AL and (b) with AL. Fig. 10A shows significant interference effects. The bright spot near the center of the phantom is due to constructive interference, while the relative null between that position and the bottom of the phantom is due to destructive interference. Fig. 10B shows some interference effects, but they are significantly less prominent than in Fig. 10A. Both patterns resemble the patterns shown in Fig. 6. Fig. 11 shows image intensity along a vertical line drawn through the center of the phantom. The curve without the AL shows three relative maxima within the sample, agreeing with the results in Fig. 7. The curve with the AL more closely resembles the field profile of a low-frequency surface coil without interference effects.

4. Conclusions

Wave interference is presented as a possible cause of B_1 related inhomogeneities. For the presented case of a

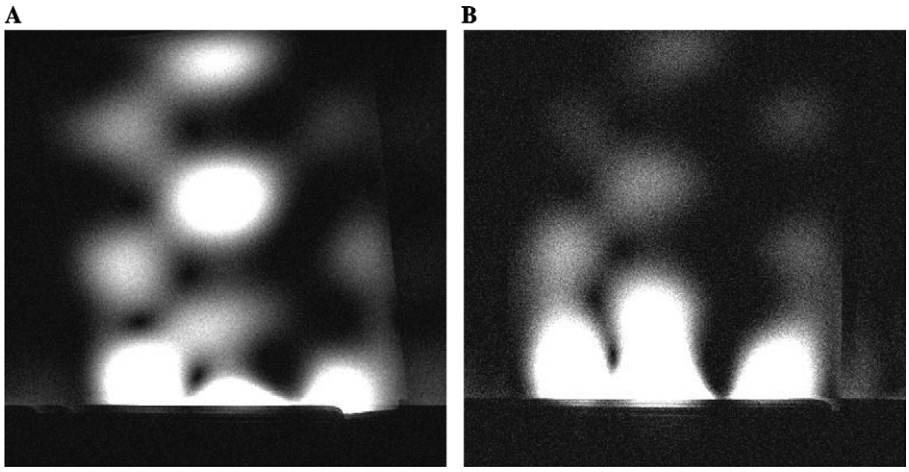

Fig. 10. T experimental images (A) without AL and (B) with AL on sides of phantom only.

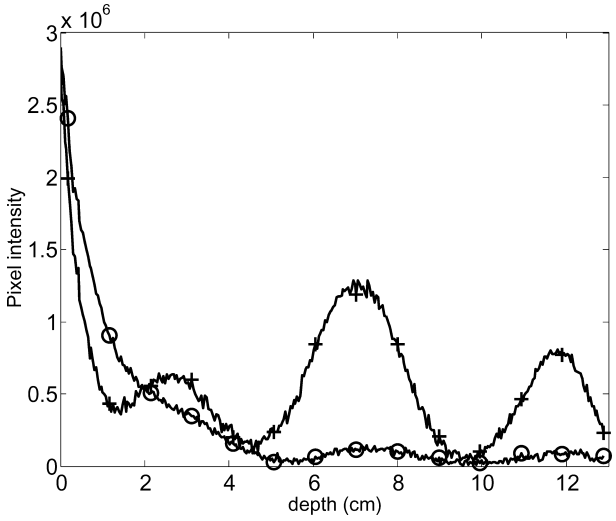

Fig. 11. Image intensity profile of experimental images, without AL showing interference effects (triangles) and with AL showing no interference effects (circles).

single surface coil, only reflected waves are available for interference. These reflections occur because of the large difference in dielectric constants between the phantom and air. Absorbing layers are presented as a method to eliminate reflected waves and reduce interference effects.

To verify the wave reflection/interference hypothesis, FDTD simulations, and 11.1 T imaging were performed with and without absorbing layers. The significant impact of the AL on both simulated and experimental images supports the hypothesis of wave interference. The strong correlation between the pairs Figs. 6A, 10A and Figs. 6D, 10B support the hypothesis and proposed solution. The reduction of wave effects creates more predictable field patterns, simplifying single-coil and array design. The minimal wave effects present when there is a gap between the sample and absorbing layer, and the SNR reduction when the absorbing layer is added warrant further investigation to optimize the absorbing layer properties—thickness, conductivity, and permittivity.

Although interference effects occur for a large range of sizes, certain sizes were most susceptible, as evidenced by the largest local SNR loss. An approach that renders the B_1 field distribution easily predictable may improve image homogeneity at high fields, decrease design time for RF coils, and also offer consistent images for various sample sizes.

B_1 inhomogeneities ultimately arise from the solution of Maxwell's equations for a given coil/load combination. Past approaches considered modifying the coil [9–11], while this work focused on modifying the load, specifically the boundary conditions, as was initially proposed in [12]. This work also reinforces the fundamental process for interference, for the case of a single surface coil—wave reflections. The strong correlation between FDTD predictions and 11.1 T experimental images strengthen the idea that the FDTD method is a practical and accurate numerical solution to Maxwell's equations for MRI applications.

Acknowledgments

We acknowledge Ray Luebbers whose description of the Perfectly Matched Layer (PML) [23] during Remcom's XFDTD training session inspired this work. We thank Wayne Bomstad for his insightful discussions, Chris Collins for this thorough critique, Kelly Jenkins for coil construction, and Steve Blackband for his assistance in preparing the manuscript. We thank Pete Michel and Walt Mickle in the UF Bioengineering Department for phantom and absorbing layer construction. MRI data were supported through the National High Magnetic Field Laboratory and obtained at the Advanced Magnetic Resonance Imaging and Spectros-

copy (AMRIS) facility in the McKnight Brain Institute of the University of Florida. We acknowledge the NIH (Grants R01:NS41094-01 and P41:RR16105) and the National High Magnetic Field Laboratory, Tallahassee, FL for grant funding.

References

[1] W.A. Edelstein, G.H. Glover, C.J. Hardy, R.W. Redington, The intrinsic signal-to-noise ratio in NMR imaging, Magn. Reson. Med. 3 (1986) 604–618.
[2] C. Gabriel, Compilation of the dielectric properties of body tissues at RF and microwave frequencies, Air Force materiel command, Brooks Air Force Base, TX, AL/OE-TR-1996-0037, 1996.
[3] C.M. Collins, Q.X. Yang, J.H. Wang, X. Zhang, H. Liu, S. Michaeli, X.-H. Zhu, G. Adriany, J.T. Vaughan, P. Anderson, H. Merkle, K. Ugurbil, M.B. Smith, W. Chen, Different excitation and reception distributions with a single-loop transmit-receive surface coil near a head sized spherical shantom at 300 MHz, Magn. Reson. Med. 47 (2002) 1026–1028.
[4] J. Wang, Q.X. Yang, X. Zhang, C.M. Collins, M.B. Smith, X.-H. Zhu, G. Adriany, K. Ugurbil, W. Chen, Polarization of the RF field in a human head at high field: a study with a quadrature surface coil at 7.0 T, Magn. Reson. Med. 48 (2002) 362–369.
[5] Q.X. Yang, J. Wang, X. Zhang, C.M. Collins, M.B. Smith, H. Liu, X.-H. Zhu, J.T. Vaughan, K. Ugurbil, W. Chen, Analysis of wave behavior in lossy dielectric samples at high field, Magn. Reson. Med. 47 (2002) 982–989.
[6] T.S. Ibrahim, R. Lee, A.M. Abduljalil, B.A. Baertlein, P.-M.L. Robitaille, Dielectric resonances and B1 field inhomogeneity in UHFMRI: computational analysis and experimental findings, Magn. Reson. Imag. 19 (2001) 219–226.
[7] D.I. Hoult, Sensitivity and power deposition in a high-field imaging experiment, J. Magn. Reson. Imag. 12 (2000) 46–67.
[8] A. Kangarlu, B.A. Baertlein, R. Lee, T. Ibrahim, L. Yang, A.M. Abduljalil, P.-M.L. Robitaille, Dielectric resonance phenomena in ultra high field MRI, J. Comput. Assist. Tomogr. 23 (6) (1999) 821–831.
[9] T.S. Ibrahim, R. Lee, B.A. Baertlein, A.M. Abduljalil, H. Zhu, P.-M.L. Robitaille, Effect of RF coil excitation on field inhomogeneity at ultra high fields: a field optimized TEM resonator, Magn. Reson. Imag. 19 (2001) 1339–1347.
[10] D.C. Alsop, T.J. Connick, G. Mizsei, A spiral volume coil for improved RF field homogeneity at high static magnetic field strength, Magn. Reson. Med. 40 (1998) 49–54.
[11] T.K.F. Foo, C.E. Hayes, Y.W. Kang, Reduction of RF penetration effects in high field imaging, Magn. Reson. Med. 23 (1992) 287–301.
[12] Q.X. Yang, M.B. Smith, H. Liu, X. Zhang, J. Wang, K. Ugurbil, W. Chen, Manipulation of signal intensity distribution with dielectric loading at 7.0 T, Proc. 9th ISMRM 9 (2001) 1096.
[13] F.T. Ulaby, Fundamentals of Applied Electromagnetics, Prentice Hall, Upper Saddle River, 1999.
[14] M. Alecci, C.M. Collins, M.B. Smith, P. Jezzard, Radio frequency magnetic field mapping of a 3 Tesla birdcage coil: experimental and theoretical dependence on sample properties, Magn. Reson. Med. 46 (2001) 379–385.
[15] R.W. Brown, E.M. Haacke, M.A. Martens, J.L. Patrick, F.R. Zypman, A layer model for RF penetration, heating, and screening in NMR, J. Magn. Reson. Med. 80 (1988) 225–245.
[16] P.A. Bottomley, E.R. Andrew, RF magnetic field penetration, phase shift and power dissipation in biological tissue: implications for NMR imaging, Phys. Med. Biol. 23 (1978) 630–643.
[17] K.S. Yee, Numerical solution of initial boundary value problems involving Maxwell's equations in isotropic media, IEEE Trans. Ant. Propag. 14 (1966) 302–307.
[18] K.S. Kunz, R.J. Luebbers, The Finite Difference Time Domain Method for Electromagnetics, CRC Press, Boca Raton, 1993.
[19] C.M. Collins, M.B. Smith, Signal-to-noise ratio and absorbed power as functions of main magnetic field strength, and definition of "90°" RF pulse for the head in the birdcage coil, Magn. Reson. Med. 45 (2001) 684–691.
[20] T.S. Ibrahim, R. Lee, B.A. Baertlein, Y. Yu, P.-M.L. Robitaille, Computational analysis of the high pass birdcage resonator: finite difference time domain simulations for high-field MRI, Magn. Reson. Imag. 18 (2000) 835–843.
[21] B. Beck, D.H. Plant, S.C. Grant, P.E. Thelwall, X. Sliver, T.H. Mareci, H. Benveniste, M. Smith, C. Collins, S. Crozier, S.J. Blackband, Progress in high field MRI at the University of Florida, MAGMA 13 (2002) 152–157.
[22] D.I. Hoult, The principle of reciprocity in signal strength calculations—a mathematical guide, Conc. Magn. Reson. 12 (4) (2000) 173–187.
[23] J. Berenger, A perfectly matched layer for the absorption of electromagnetic waves, J. Comp. Phys. 114 (1994) 185–200.